AD_____

AWARD NUMBER: W81XWH-05-1-0363

TITLE: Miniature and Molecularly Specific Optical Screening Technologies for Breast Cancer

PRINCIPAL INVESTIGATOR: Nimmi Ramanujam, Ph.D.

CONTRACTING ORGANIZATION: Duke University
Durham, North Carolina 27710

REPORT DATE: October 2006

TYPE OF REPORT: Annual

PREPARED FOR: U.S. Army Medical Research and Materiel Command
Fort Detrick, Maryland 21702-5012

REPORT DOCUMENTATION PAGE

Form Approved
OMB No. 0704-0188

1. REPORT DATE *(DD-MM-YYYY)*	**2. REPORT TYPE**	**3. DATES COVERED** *(From - To)*
01-10-2006	Annual	1 Sep 2005 – 31 Aug 2006

4. TITLE AND SUBTITLE

Miniature and Molecularly Specific Optical Screening Technologies for Breast Cancer

5a. CONTRACT NUMBER

5b. GRANT NUMBER
W81XWH-05-1-0363

5c. PROGRAM ELEMENT NUMBER

6. AUTHOR(S)

Nimmi Ramanujam, Ph.D.

E-Mail: nimmi@duke.edu

5d. PROJECT NUMBER

5e. TASK NUMBER

5f. WORK UNIT NUMBER

7. PERFORMING ORGANIZATION NAME(S) AND ADDRESS(ES)

Duke University
Durham, North Carolina 27710

8. PERFORMING ORGANIZATION REPORT NUMBER

9. SPONSORING / MONITORING AGENCY NAME(S) AND ADDRESS(ES)
U.S. Army Medical Research and Materiel Command
Fort Detrick, Maryland 21702-5012

10. SPONSOR/MONITOR'S ACRONYM(S)

11. SPONSOR/MONITOR'S REPORT NUMBER(S)

12. DISTRIBUTION / AVAILABILITY STATEMENT
Approved for Public Release; Distribution Unlimited

13. SUPPLEMENTARY NOTES

14. ABSTRACT

The goal of this proposal is to harness the power of light to create "miniature and molecularly specific optical technologies" for breast cancer diagnosis and detection. The miniature technologies will leverage on millimeter scale silicon detectors and LEDs to make compact devices that can be used in a practical clinical setting for breast cancer detection. The features that will be exploited for optical detection/diagnosis of breast cancer will include the physiological, structural and molecular alterations that accompany the transformation of a cell from a normal to malignant state.

15. SUBJECT TERMS
optical, spectroscopy, imaging, fiber-optic, molecular, screening

16. SECURITY CLASSIFICATION OF:			**17. LIMITATION OF ABSTRACT**	**18. NUMBER OF PAGES**	**19a. NAME OF RESPONSIBLE PERSON**
a. REPORT	**b. ABSTRACT**	**c. THIS PAGE**			USAMRMC
U	U	U	UU	21	**19b. TELEPHONE NUMBER** *(include area code)*

TABLE OF CONTENTS

1 INTRODUCTION

The goal of this proposal is to harness the power of light to create "miniature and molecularly specific optical technologies" for breast cancer diagnosis and detection. The miniature technologies will leverage on millimeter scale silicon detectors and LEDs to make compact devices that can be used in a practical clinical setting for breast cancer detection. The features that will be exploited for optical detection/diagnosis of breast cancer will include the physiological, structural and molecular alterations that accompany the transformation of a cell from a normal to malignant state.

2 BODY

2.1. Project 1: System-on-a-chip device:

The goal is to build a miniature device that can perform diffuse reflectance spectroscopy of breast tissues in the visible spectral range between 350-600 nm. The measured spectra will be processed using an inverse Monte Carlo model to extract optical properties (absorption and scattering) which reflect the physiological (total hemoglobin content and hemoglobin saturation) and structural properties of breast tissues.

Statement of work for year 1

To establish the design specifications of the first-generation system-on-a-chip device. This aim will involve throughput calculations and Monte Carlo modeling to determine the signal-to-noise ratio that can be achieved with the micro scale sources and detectors, and the experimental evaluation of the signal-to-noise of the test system on turbid "tissue-like" media. The signal-to-noise ratios achieved with the test system will be quantitatively compared to that achieved with a standard bench top system (year 1).

Accomplishments in year 1

This section describes the research accomplishments associated with each task outlined in the above Statement of Work (SOW). The major achievements include thermal modeling of the heat dissipation effects of compact LEDs on tissue samples, selection of multiwavelength compact light sources, calculating bandwidth effects of broadband light sources (such as LEDs) on the RMS errors for the extracted tissue optical and physiological properties, selection of photodiodes, and the design and testing of various single-pixel probe prototypes.

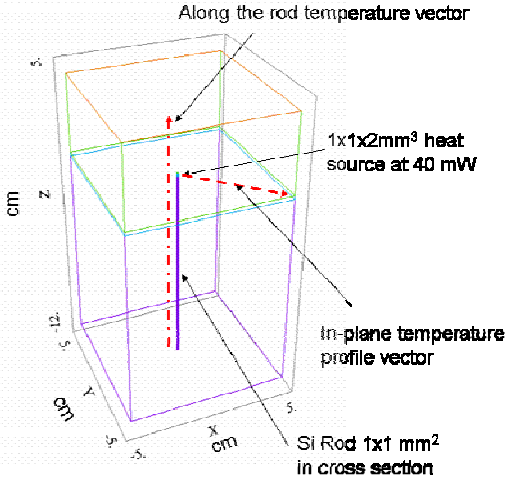

Figure 1: Schematic of modeled region

1.1.1 Thermal modeling

The compact size of the integrated probe has several implications in terms of the dissipation of heat from the local light sources. LEDs as a compact light source are not 100% efficient and there is waste heat generated which will be dissipated into the surrounding tissue. The impact of this waste heat was studied through simulation and modeling. The modeled structure consisted of a compact source, 2 mm^3 on a silicon rod of 1 mm^2 cross-section as shown in Figure 1. Typical power levels (40 mW) and efficiencies were assumed in the model. The thermal conductivity of breast tissue was taken from the literature [1]. A time transient analysis was performed over a period of 10 minutes. This is considered longer than any expected measurement time and is considered an upper bound to the temperature rise. The results of this model are summarized in Figure 2 and 3. The maximum temperature rise expected near the probe or source tip is less than 3° for this model and geometry. This model indicates that the suggested probe sources and geometry are well suited to the application and well-within constraints of tissue compatibility.

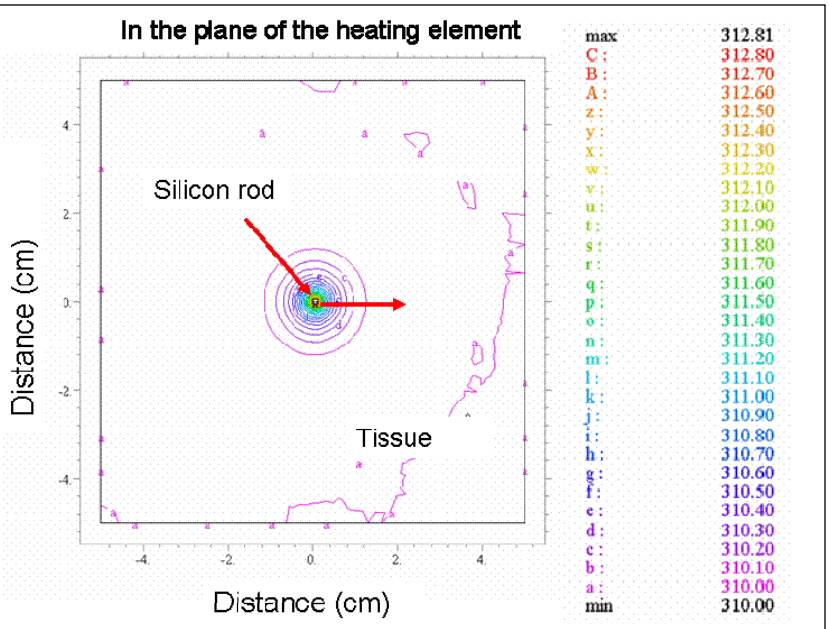

Figure 2: The in-plane temperature profile within tissue away from the LED source. The scale refers to the temperature in °K.

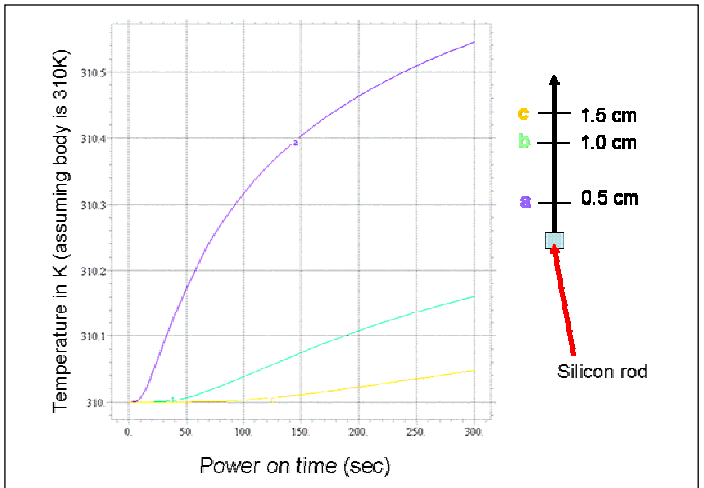

Figure 3: The temperature profile as a function of time at specific distances from the probe tip.

2.1.2. Light source

The light source requirements are a tunable source that emits in the visible wavelength range between 350-600 nm. This will be consistent with the tenability of the bench top system employed currently by our group for breast tissue optical spectroscopy studies.

A. Multi-Wavelength LED Package

It is of great advantage to use a multi-wavelength LED as the light source for the miniature sensor array. First, multi-wavelength LEDs can be easily mounted on to a single substrate

with photodiodes, eliminating the need of optical fibers in construction of a miniature sensor array. Second, LEDs are less sensitive to temperature changes than laser diodes which require delicate thermal management. Third, LEDs are more stable in emission power and spectrum. Finally, they are less expensive than laser diodes.

The OTLA-0100 from Opto Technology Inc. (www.optotech.com) is a commercially available multi-wavelength illuminator with nine LED chips packaged into a compact, thermally conductive ceramic substrate. It offers wavelengths that range from Ultra Violet through the Visible Red Spectrum (383 – 700 nm) and output power from 0.8-5.3 mW. Opto Technology also designs custom chip on board assemblies with single and multiple wavelengths of UV, Visible and IR LED die (365 – 940 nm), custom filters, photo detectors, optics, heat sinks and custom packages.

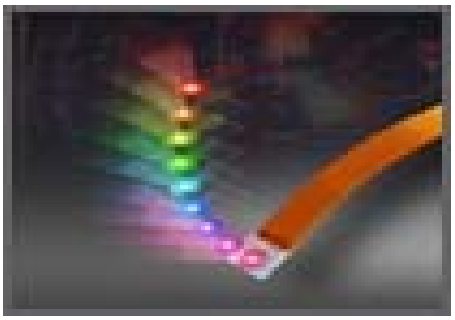

Figure 4. Picture of an OTLA-0100 multi-wavelength illuminator.

The major features of the multi-wavelength LEDs include:

- Wavelengths can be individually controlled
- Small source size ideal for coupling of secondary focusing optics
- Can be customized with different wavelengths

One of the challenges using the multi-wavelength LEDs is to optimize the layout of the individual LED dies on the sensor substrate so that they have the same distance to the photodiode, which may significantly ease the data analysis. Optimized layout will also reduce the space needed for the interface between the LEDs and their drivers.

B. Multi-wavelength visible laser

An alternative light source is a multi-wavelength cavity stabilized visible laser system developed by Ahura Corporation (http://www.ahuracorp.com). In this system, cavity stabilized lasers are designed as plug-in cards to a multi-laser platform. Available wavelengths include: 405, 440, 470, 490, 510, 530, 550, 570, 590, 610, 630 and 650 nm. Wavelength multiplexing is available to combine all wavelengths into a single fiber.

Figure 5. Picture of a multi-wavelength cavity stabilized visible laser system from Ahara.

The multi-wavelength cavity stabilized visible laser system has many unique features, including:

- Up to 10 colors between 430 -670 nm
- Output optical power up to 50 mW
- Output Power Stability <1% peak-to-peak
- High semiconductor reliability
- Low power consumption
- Wavelength multiplexer
- High speed modulation
- Digital intensity control
- Control USB Interface and LAN & wireless

Ahura's multi-wavelength laser system greatly reduces the overall instrument size, reduces fiber management complexities, and increases the overall performance and functionality of the system. The source optical fiber can be brought very close to the active area of a photodiode. The small source-detector separation can remarkably boost the collection efficiency and therefore signal-to-noise ratio. However, the use of optical fiber as illumination source will also bring some challenges in fabrication of a sensor array. More investigation is required on how to arrange tens or even hundreds of source fibers on a single chip and on how to divide or switch optical power among these fibers.

C. Custom LEDs

We have worked with a leading manufacturer of LEDs, Lumileds, to create specific mounted LEDs for our application. The diodes are of the wavelengths: 420, 40, 470, 540 and 560 nm. We are designing a Si wafer-scale mount for these devices in order to co-locate several individually addressed LEDs. These devices will offer increased flexibility as well as compact packaging.

2.1.3. Bandwidth effects

Because LEDs have a larger bandwidth than the conventional bench top system we have employed previously, a series of simulations were carried out to evaluate the effects of the larger bandwidth, on the accuracy with which optical properties and hemoglobin content and saturation can be extracted. This was done using Monte Carlo simulations to model the diffuse reflectance

that would be measured using a variety of instrument characteristics, and using a Monte Carlo inverse model to then extract the optical properties from these simulated spectra.

The simulated spectra were generated using Mie theory to model scattering, and using a range of oxy and deoxy-hemoglobin concentrations to generate the absorption coefficients. In order to approximate a realistic measurement, noise was added to each simulated data point to obtain an SNR of 25, which is reasonable based on our preliminary measurements. Finally, a Gaussian smoothing function, having a full width at half maximum (FWHM) ranging from 5 to 30 nm, was applied to the data, using a moving average to evaluate the effects of the bandwidth of the LEDs. Finally, an inverse Monte Carlo based diffuse reflectance model was applied to these data, to determine the accuracy with which the optical properties (and hence, tissue physiological and structural properties) could be extracted. 5 discrete wavelengths were used in the inversion (405, 430, 470, 505, and 570 nm), since this is a reasonable number that could be used in a physical device.

Table 1 shows the results of these inversions. The bottom row corresponds to the measurements obtained by the current bench top system, consisting of measurements at 41 wavelengths ranging from 400-600 nm. The bandwidth can be seen to have a negligible effect on the accuracy with which the absorption coefficient (μ_a) and reduced scattering coefficient (μ_s') can be extracted, while increasing the number of wavelengths from 5 (first five rows of data) to 41 (bottom row) can be seen to reduce the error by approximately a factor of two. The error in the extracted total hemoglobin content shows a similar trend, while the error in hemoglobin saturation shows a moderate increase as the bandwidth is increased. These results indicate that the spectral data obtained using an LED based device are suitable for extraction of optical properties using algorithms developed for the bench top system.

Table 1: The RMS errors for the extracted optical properties and hemoglobin content and saturation are shown for a range of illumination characteristics. It can be seen that the bandwidth has no effect on the accuracy with which optical properties and total Hb can be extracted, and a small effect on the accuracy with which Hb saturation can be obtained.

Bandwidth	***RMS Error μ_a (cm^{-1}), Range 0-21***	***RMS Error μ_s' (cm^{-1}), Range 2-27***	***RMS Error Total Hb (μM), Range 0.2-20***	***RMS Error Hb StO_2 (%), Range 1-99***
30	0.3	0.7	0.7	16.7
20	0.3	0.7	0.7	14.7
15	0.3	0.8	0.7	12.6
10	0.3	0.7	0.7	12.3
5	0.3	0.7	0.8	12.8
5: Wavelengths-(400:5:600)	0.15	0.3	0.4	9.8

2.1.4. Detectors

We have initiated work on the detector performance and integration using commercially available, small area detectors. We have used two sizes of detectors: 1x1 mm^2 and 4x4 mm^2. These Si photodiodes were used in a variety of configurations. Initial baseline measurements were completed and discussed below on the packaged detector. We have modified these detectors in several configurations for use on the platform. These configurations are:

D1: Sealed detector (P1), 1x1 mm^2 area
D2: Unsealed detector (P2), 1x1 mm^2 area, wherein the cap and window regions of the package were removed allowing for the direct use of the photodetecter without the hermetic sealed package.
D3: Unsealed 1 mm^2 detector with a hole drilled next to the die in the base to allow the close location of the light source to the detector to maximize collection efficiency.
D4: Unsealed large area, 4x4 mm^2, detector with *and* without a hole mechanically drilled through the center of the die for the placement of the excitation in the die center.

Additional configurations will be explored including the use of selective etches to chemically generate the center hole in the Si photodiode without the creation of mechanical damage which could degrade the performance of the Si detector.

2.1.5. Single-pixel probe

A. Probe design

We have designed four single-pixel probe geometries P1-P4, shown in Figure 6, and have completed the construction and test of first two probe geometries (P1 and P2).

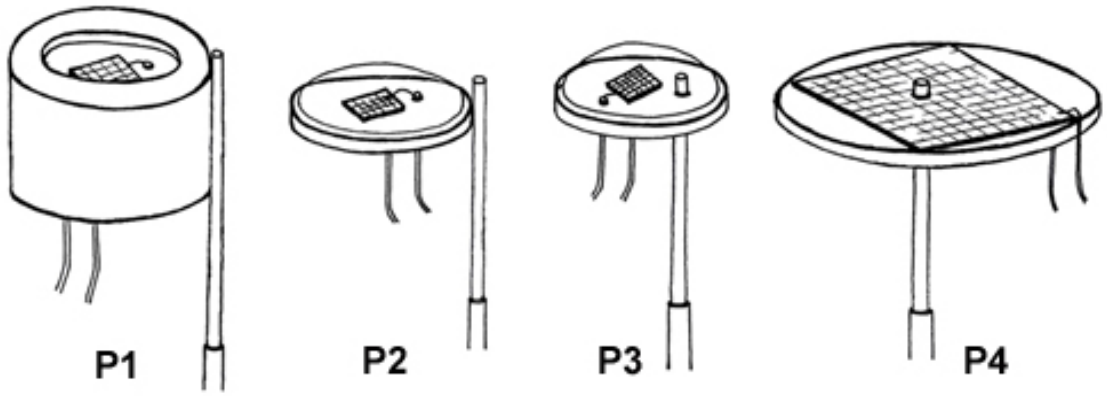

Figure 6. Conceptual drawings of four single-pixel probe geometries P1-P4.

In the first single-pixel probe geometry P1, a 600/660/710 μm source optical fiber is directly glued to the outer side of the sealed detector D1 with the fiber tip in the same plane of the detector window. The distance between the fiber tip and the center of the detector window is 2.9 mm and the window is about 2 mm from the detector die. This geometry results in a minimum source-detector separation of 4.9 mm. P1 was mounted on a 20 mm x 20 mm PCB board, shown in Figure 7a.

P2 consists of a 600/660/710 μm source optical fiber and the unsealed 1x1 mm^2 detector D2. The fiber tip is in the same plane of the detector active area, resulting in a source-detector separation of 2.3 mm. P2 was packaged into a plastic tube of 10 mm diameter, shown in Figure 7b. To protect the exposed detector die and the fiber tip from any damage, a thin layer of biocompatible epoxy (EPO-TEK 301) was applied to cover the die and the fiber tip.

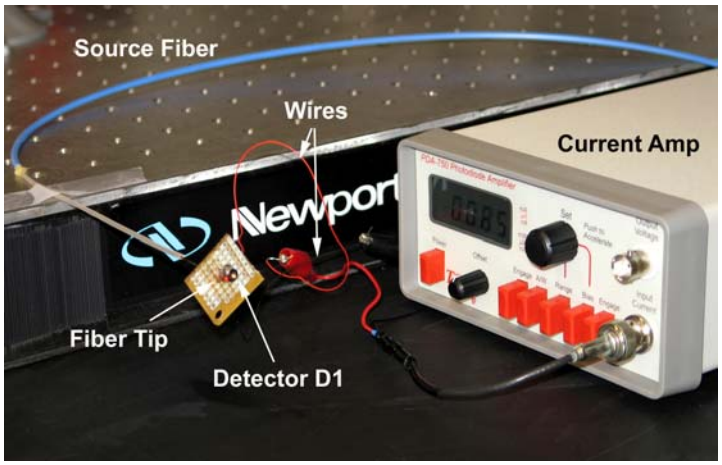

(a)

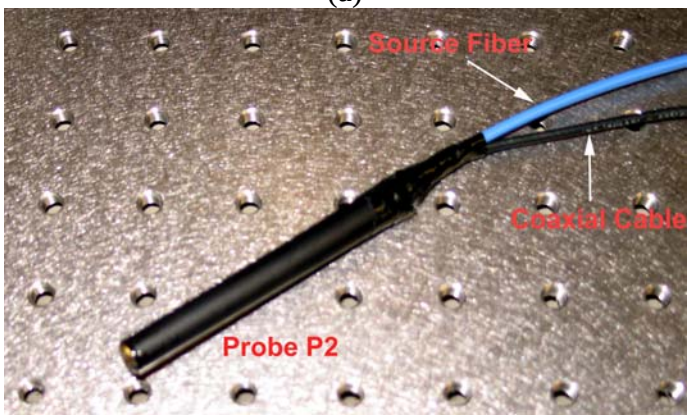

(b)

Figure 7 Picture of the single-pixel probe prototype (a) P1 and (b) P2.

Probe P3 is to be built with the detector D3, in which a 600/660/710 μm source optical fiber will be inserted into the drilled hole next to the detector die in the base. The fiber tip and the die will be in a same plane, resulting in a source-detector separation of 1.9 mm.

Probe P4 will be built using a 600/660/710 μm source optical fiber and the detector D4 with a hole drilled through the center of the die. This geometry has the largest collection area and smallest separation, therefore, is expected to provide the best signal-to-noise ratio.

B. Probe Test

To test the performance of the prototype single-pixel probes, four Intralipid and ink phantoms A-D, from darkest to lightest and representing breast tissue optical property ranges in the 400-600 nm band, were used. Since a 660 nm laser diode was used for the tests, the optical properties of the phantoms in Table 2 are given at this wavelength. The illumination power out of the source fiber is 1.0 mW at 660 nm. A PDA-750 photodiode transimpedance amplifier from Terahertz Technologies Inc. was employed to measure the detector output current. In the phantom experiments, the tip of the source fiber was in contact with the phantom surface, simulating a semi-infinite geometry. Room lights were reduced to make the room dark. In fact, room lights have negligible effects on all the measurements due to the sufficient phantom volume used. The results are summarized in Table 2, in which the leakage current was measured in distilled water.

Table 2: Measured output current and drift of the probes in different tissue phantoms and probe leakage in distilled water. The illumination power at 660 nm is 1.0 mW.

Probe	**Phantom A** $\mu a=15\ cm^{-1}$ $\mu s'=20\ cm^{-1}$	**Phantom B** $\mu a=15\ cm^{-1}$ $\mu s'=5.0\ cm^{-1}$	**Phantom C** $\mu a=2.0\ cm^{-1}$ $\mu s'=20\ cm^{-1}$	**Phantom D** $\mu a=2.0\ cm^{-1}$ $\mu s'=5.0\ cm^{-1}$	**Leakage Current**
P1 (nA)	11.3 ± 0.5	35.5 ± 0.5	540 ± 8	1410 ± 20	$I_{Leak}\approx 0$
P2 (μA)	1.405 ± 0.005	1.635 ± 0.035	5.595 ± 0.035	6.365 ± 0.165	$I_{Leak}=0.38$
P3	N/A	N/A	N/A	N/A	N/A
P4	N/A	N/A	N/A	N/A	N/A

For P1, a signal-to-noise ratio of 22 for the darkest phantom (phantom A) and 70 for the lightest phantom (phantom D) were achieved. Due to the shielding effects of the detector cap, the light leakage directly from the source fiber to the detector is negligible. The major sources of noise include the detector dark current, the shot noise and the amplifier noise. We also investigated the output linearity of the probe with varying illumination optical power and the result is shown in Figure 8. The laser diode operated in its linear range during the experiment, i.e., its output optical power linearly depends on the applied driving current. Obviously, P1 has very linear response to the illumination power within the measured range (< 40 mW).

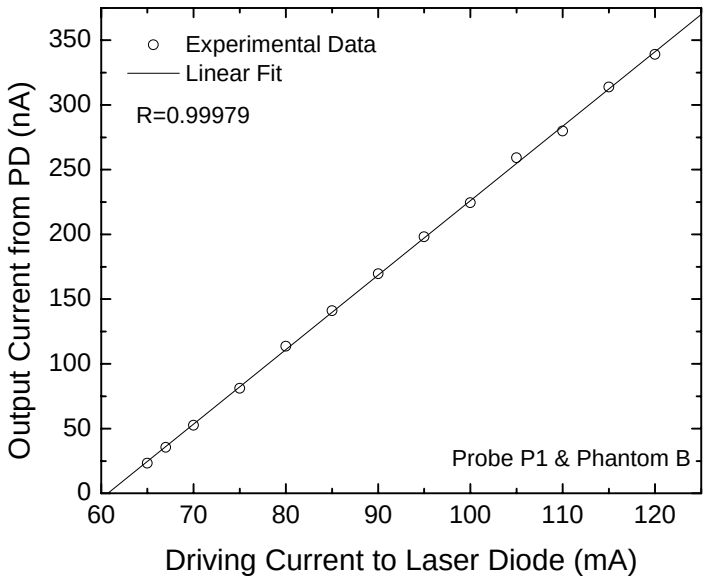

Figure 8 Probe output current linearity.

Two to three orders of magnitude higher optical signal was detected by P2 compared with that detected by P1. This is mainly attributed to the significantly reduced source-detector separation and the removal of the detector cap, which otherwise blocks most of the photons from reaching the detector die. However, the price for the high signal level is that the light leakage is also orders higher than that of P1. The scattering of the unpolished fiber endface and the epoxy are believed to be the major sources of light leakage. The scattering can be reduced by polishing the fiber tip using very fine polishing films. Leakage due to the epoxy was caused by air bubbles within the epoxy and the refractive index mismatch between the epoxy (n≈1.53 @660 nm) and the liquid phantom (n≈1.33 @660 nm). Two solutions may solve the epoxy effects: adding an absorptive baffle plate in between fiber tip and the detector or keeping the fiber tip epoxy free. We will investigate all these three approaches in the coming months.

P3 and P4 will also be built and tested in the same batch of Intralipid phantoms. A more comprehensive comparison between the four probe geometries will be performed and the best one will be selected for *in vivo* mouse studies and *ex vivo* breast tissue studies.

2.2. Project 2: Physiologic, metabolic and molecular characterization of breast cancer in an animal model of breast cancer (aim 2)

The goal is to validate the use of optical spectroscopy techniques to quantify the physiological properties of breast cancer. Validation studies were carried out on an animal model of breast cancer undergoing a perturbation using carbogen inhalation.

Statement of work for year 1
Physiological and metabolic characterization of mammary tumors in an animal model of breast cancer. Nude mice will be injected in the flank with 500,000 4T1/D2 cancer cells. The tumors

will be allowed to grow until they have reached a size of approximately 8 mm in diameter (approximately 1-2 weeks). Non-invasive optical measurements of tumor oxygenation, vascularity and metabolism will be measured using a continuous wave system and compared to independent measurements of tumor hypoxia using an OxyLite fiber optic sensor and immunohistochemistry of hypoxic and metabolic markers.

Accomplishments in year 1

Over the past year, we have carried out work related to task 2a, in accordance with our statement of work. The goal of this task is to demonstrate the feasibility of dynamically monitoring tissue physiological parameters *in vivo* using optical spectroscopy. Non-invasive optical spectroscopy was performed on 4T1 breast tumors grown in the flank of nude mice (n=10) before and after the administration of carbogen (95% O_2, 5% CO_2), by placing a fiber optic probe in contact with the surface of the tumor, as shown in Figure 9. Two Oxylite pO_2 sensors (Oxford Optronix, Oxford, UK) inserted into tumor were used as the gold standard. Two sets of optical measurements were made, the first being the diffuse reflectance spectra, which was acquired over the wavelength range 350-600 nm. A Monte Carlo model of light transport was then used to determine the absorption and scattering properties of the tissue, including the hemoglobin concentration and saturation [2]. The second set of measurements was the fluorescence emission spectra obtained at 350 and 460 nm excitation. These correspond to the peak fluorescence excitation wavelengths of the electron carriers NADH and FAD, respectively. These data were also analyzed using Monte Carlo-based model of fluorescence, to extract the relative fluorophore concentrations, independent of the effects of absorption and scattering, as described below.

Figure 10 shows representative plots of tissue pO_2, hemoglobin (Hb) saturation, and total Hb

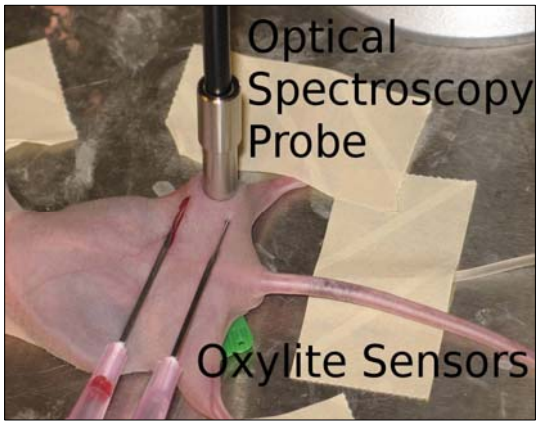

Figure 9. Experimental setup showing the placement of the optical spectroscopy probe and Oxylite sensors.

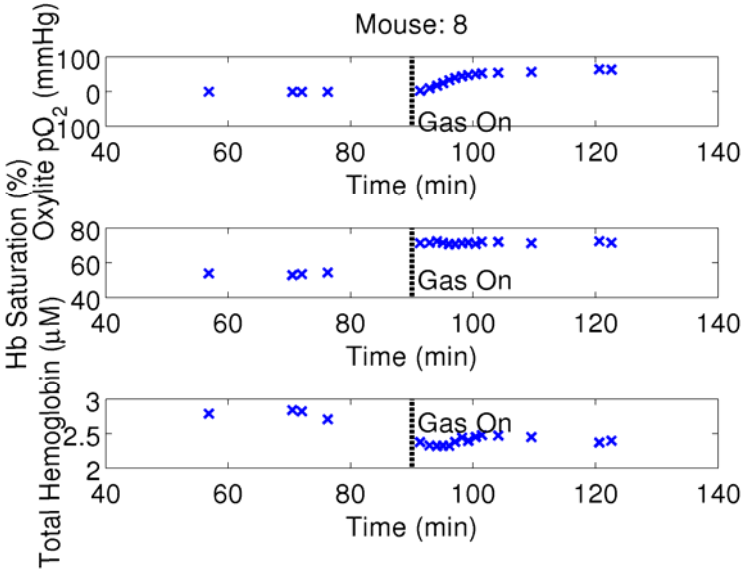

Figure 10. pO_2, Hb saturation, and total Hb measured as a function of time upon carbogen administration at t=90 minutes.

content for 1 animal. It can be seen that the administration of carbogen elicits an increase in both tissue pO_2 and Hb saturation, as assessed by the Oxylite sensors and optical spectroscopy, respectively. It can be seen that the Hb saturation shows a more rapid response to the administration of carbogen at t=90 minutes, which was found to be typical of other mice as well. The correlation coefficient between the Oxylite and Hb saturation measurements was 0.71. It can also be seen that the total Hb content decreases slightly upon carbogen administration, although this change was not seen consistently.

Figure 11 shows the hemoglobin saturation, Oxylite pO_2, total hemoglobin content, and redox ratio (NADH/FAD fluorescence) for the case before (blue) and after (red) carbogen administration. For the treated (red) group only those data points collected at least 10 minutes after the start of carbogen were included, as this was approximately the time when the measurements stabilized. For the set of 10 animals, a significant increase was seen in pO_2 reported by the Oxylite system ($p<0.05$), and Hb saturation reported by optical spectroscopy ($p<0.001$), using a paired t-test. Significant differences were also seen using unpaired t-tests for pO_2 ($p<0.05$) and Hb saturation ($p<0.005$). This is consistent with what is expected. Using the Oxylite sensors enables us to identify consistent trends in these data, however due to the nature of these measurements it is difficult to compare them in absolute terms. Of particular difficulty is the small sampling volume of the Oxylite probes, which makes the Oxylite sensors highly sensitive to localized changes in pO_2 (the two sensors frequently differed from each other by a factor of two or more). Furthermore, one or both of the Oxylite probes frequently reported no change in pO_2, remaining at approximately 0 mmHg throughout the experiment. This is likely a result of the sensors being placed in a poorly perfused or necrotic region of the tissue. For the purpose of these plots, when one Oxylite exhibited this, only the data from the other Oxylite was used, in all other cases they were averaged.

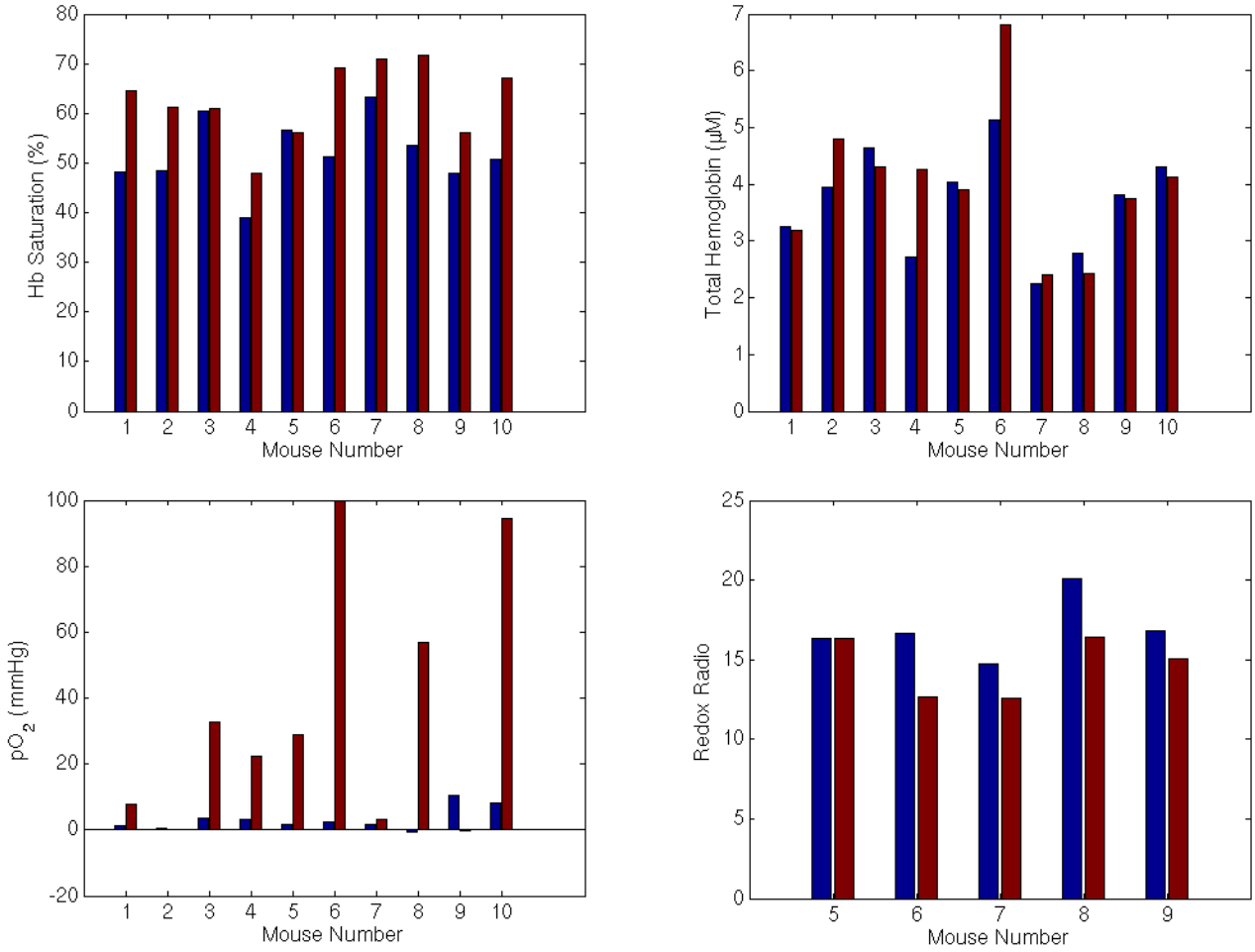

Figure 11. The hemoglobin saturation, total hemoglobin content, Oxylite pO_2, and redox ratio (NADH/FAD fluorescence) are shown for baseline (blue) and after carbogen administration (red).

Finally, the redox ratio is the last graph of Figure 11. This is the ratio of intrinsic fluorescence, i.e. the fluorescence intensity corrected for the effects of absorption and scattering using Monte Carlo modeling tools our group has previously developed (manuscript in preparation). In the presence of oxygen, the redox ratio would be expected to decrease [3], as is shown for four of the five cases. For the case where the redox ratio did not decrease, it is interesting to note that the Hb saturation also did not change significantly upon carbogen administration (mouse 5), so the data are consistent using two independent measures of tumor physiology. A paired t-test indicates that there is a significant reduction in the redox ratio upon the administration of carbogen ($p<0.05$), while an unpaired t-test test yields $p<0.1$. Thus, optical spectroscopy was found to track expected physiologic changes in Hb saturation and metabolic redox ratio upon administration of carbogen.

Finally, we are also in the process of processing and analyzing immunohistochemistry markers of hypoxia to further correlate these measurements with hypoxic fraction as reported by pimonidazole and HP24 staining. Due to the technical difficulties of developing the double

staining technique for reporting hypoxic fraction at two time points on a single tissue specimen, the results have not been fully analyzed. However, we have successfully completed a double staining protocol on a set of histology slides from these tumors, and examples of these findings are shown in Figure. 12. The left side of Figure 12 shows pimonidazole staining, which indicates the hypoxic fraction while the animal is breathing room air (higher intensity indicates lower pO_2), while the right image shows HP24 staining, which indicates the hypoxic fraction during carbogen breathing in a similar way. We expect further analysis of these images to provide better spatial correlation between the optical measurements and the independent measure of hypoxia, and potentially yield a more reliable standard with which to compare.

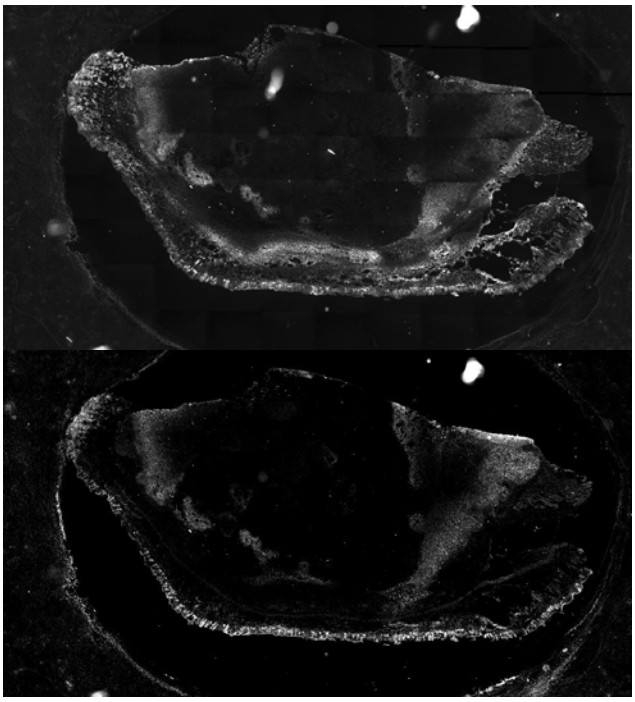

Figure 12. Pimonidazole (top) and HP24 (bottom) images acquired from a single tissue specimen. Brighter fluorescence intensity indicates lower pO_2. It can be seen that a larger fraction of the tissue sample is fluorescence in the pimonidazole image, indicating a larger hypoxic fraction while breathing room air, than carbogen.

3 KEY RESEARCH ACCOMPLISHMENTS

During the last 12 months, following major achievements have been accomplished:

- We simulated the thermal effects of LEDs on tissue samples and a maximum temperature rise expected near the probe or source tip is less than 3°.
- We conducted component searching, selection, and customized design of light sources and detectors for both single-pixel probes and probe arrays.
- Monte Carlo simulation was performed to simulate the effects of the finite LED bandwidth on the extracted optical and physiological properties.

- Four single-pixel probe geometries (P1-P4) have been designed with P1 and P2 been built and tested using tissue phantoms. Good signal-to-noise ratio and excellent linear response have been achieved for the first two prototype probes.
- Validated the ability of optical spectroscopy to consistently monitor changes in tumor physiology, including tissue oxygenation (as assessed by Hb saturation), and metabolic redox ratio.
- Established double staining protocol to enable assessment of tumor hypoxia at two time points on the same tissue slice.

4 REPORTABLE OUTCOMES

Results from Project 2, including the perturbation validation studies in murine models described above, will be presented in an invited talk at the Optical Society of America Frontiers in Optics 2006/Laser Science XXII joint national meeting, on October 8-12, 2006 in Rochester, NY. The presentation is entitled, "Physiologic, Metabolic, and Structural Alterations in Breast Cancer: Assessment via Optical Technologies." A short paper will be published in the conference proceedings.

5 CONCLUSIONS

The work carried out in project 1 has demonstrated the safety, and technical feasibility of developing miniature sensors for obtaining optical spectra. We have established that optical sensors consisting of photodiode detectors and fiber based illumination can measure diffuse reflectance with high signal to noise for optical properties typical of tissue in the UV-VIS. We have furthermore investigated the potential use of LEDs as light sources, by establishing their safety and characterized their impact on the modeling accuracy. These technologies would greatly reduce the size, cost, and complexity of the instrumentation required for conducting optical spectroscopy measurements in tissue, thus making this a viable clinical tool.

The work carried out on in project 2 has established to ability of optical spectroscopy to consistently track changes in tumor physiology in response to a perturbation. It was found that optical spectroscopy may in fact provide a more robust assessment of tissue oxygenation than the existing Oxylite system, likely due to its larger probing volume. This work establishes optical spectroscopy as a viable tool to monitor changes in tumor physiology in response to other treatments, including radiation, chemotherapy, and molecular therapies, offering many advantages over existing technologies. In particular, it is fast, non-invasive, quantitative, and probes a wide range of physiologic parameters, including blood content, oxygenation, and cellular metabolism.

6 REFERENCES

[1] L. Hu, A. Gupta, J. P. Gore, and L. X. Xu, "Effect of forced convection on the skin thermal expression of breast cancer," *J Biomech Eng*, vol. 126, pp. 204-11, 2004.

[2] G. M. Palmer and N. Ramanujam, "Monte Carlo-based inverse model for calculating tissue optical properties. Part I: Theory and validation on synthetic phantoms," *Appl Opt*, vol. 45, pp. 1062-71, 2006.

[3] B. Chance, B. Schoener, R. Oshino, F. Itshak, and Y. Nakase, "Oxidation-reduction ratio studies of mitochondria in freeze-trapped samples. NADH and flavoprotein fluorescence signals," *J Biol Chem*, vol. 254, pp. 4764-71, 1979.

APPENDIX

Appendix A: List of Components Available in the Market

Components available for a single-pixel probe

1) Light Sources

Opto Technology, Inc. (www.optotech.com)
Multi-wavelength illuminator OTLA-0100
Number of wavelength: 9 LED chips
Wavelength range: 365 - 940 nm (Standard & Custom wavelength)
Output power: 0.8 ~ 5.3 mW / each

J.Y. Horiba
A 450-W xenon lamp & a scanning double-excitation monochromator
UV-Visble

*Epitex (*http://www.techmark.nl/epitex/products/l660-805-1200-1300-35B32.htm)
Multi-wavelength LEDs
Bare LED Dies
Wavelength range: 430 – 1550 nm
Output power: > 100 mW

Ahura Corp.(www.ahuracorp.com)
Multi-wavelength Photonic Microsystem
Benchtop lasers w/ fiber
Number of wavelength: 3-10
Wavelength range: 430-670 nm
Output power: 5, 20, 50 mW in total
w/ USB/Lan/wireless interface

OZ Optics
White light laser sources
Benchtop lasers w/ fiber
Number of wavelength: 3
Wavelengths range: 405 – 685 nm
Output power: 0 – 15 mW / each

2) Detector

Hamamatsu
S6468 Si PIN with preamp
S8664 APD

3) Source Drivers

Ahura and OZ sources: stand alone systems. No separate drivers are needed.

Opto Technology and Epitex LED arrays: can be driven sequentially by a single current source w/ an electronic switch.

BW Tek, Inc.
BWDT-8-OEM multichannel diode laser driver board

4) Detector drivers

Terahertz Technologies Inc. (http://www.terahertztechnologies.com/)
PDA-750 Photodiode Transimpedance Amplifier
8 Decade Dynamic Range
Less than 1 pA noise
1 part in 20,000 Resolution
Analog output voltage proportional to current input
Full scale input range of +/- 20 nA to +/- 20 mA
Variable bias is digitally selectable from - 14V to + 14V
Bi-directional Rs-232 serial port

Hamamatsu
C9329 photosensor amplifier
RS-232

Electro Optical Components, Inc.
OE-200 photoreceiver

Oriel (Newport)
70710 Current Preamplifier

5) Probe Packaging
In-house probe packaging

Components available for a probe array

1. Light Sources

Opto Technology, Inc
Same as the single-pixel

Epitex
Same as the single-pixel

2. Detector
   Same as the single-pixel

3. Source Drivers
   Ahura and OZ sources: stand alone systems. No separate drivers are needed.

   Opto Technology and Epitex LED arrays: can be driven sequentially by a single current source w/ an electronic switch.

   BW Tek, Inc.
   BWDT-8-OEM multichannel diode laser driver board

4. Detector drivers

   Hamamatsu
   C9004 driver circuit for Si photodiode array
   16-ch readout
   On-board A/D converter

5. Probe Packaging

   Opto Technology, Inc
   Design custom chip on board assemblies with multiple wavelengths of UV - NIR LED die, custom filters, photo detectors, optics, heat sinks.

   Others: Any optoelectronics companies or Labs